JOURNAL OF MATERIALS SCIENCE **38** (2003) 235–243

Finite element analysis of vickers indentation cracking processes in brittle solids using elements exhibiting cohesive post-failure behaviour

A. MUCHTAR
Mechanical and Materials Engineering Department, University Kebangsaan Malaysia,
43600 Bangi, Malaysia

L. C. LIM*, K. H. LEE
Department of Mechanical Engineering, National University of Singapore,
10 Kent Ridge Crescent, Singapore 119260, Republic of Singapore
E-mail: mpelimlc@nus.edu.sg

The cracking processes during the indentation test of brittle solids is simulated by means of the finite element method (FEM) using elements exhibiting cohesive post-failure behaviour and alumina as the model material. The results show that at low indentation loads, median cracks could nucleate at full loading but Palmqvist cracks only nucleate in the unloading stage and that they may not join up even after full unloading. Such cracks are stable as they are embedded in a region of high hydrostatic compression throughout the indentation test. At high indentation loads, both median and Palmqvist cracks nucleate early during the loading stage and coalesce to form a half-penny crack on further loading. Although the cracks are embedded in a region of high hydrostatic compression during loading, an annular tensile region eventually develops in between the cracked material beneath the indenter and the surrounding uncracked material during the unloading stage of the macro-indentation. This not only provides the driving force for existing cracks to grow but also new crack systems to form. The present work shows that for brittle solids with negligible plastic deformation, the mismatch in elastic recovery between the cracked and uncracked bodies on unloading plays an important role in indentation fracture processes.

1. Introduction

Under controlled conditions, a sharp indenter produces well-defined cracks in brittle solids leaving surface radial traces that can be observed using an optical microscope without too much difficulty [1]. Fig. 1a to d show the four major crack systems produced by a Vickers pyramidal indenter, the most commonly used system. Palmqvist or radial cracks form at apexes of the indentation impression remaining connected to the surface (Fig. 1a). Median cracks are generated beneath the indentation impression (Fig. 1b). They are in the shape of a penny and lies on a plane of symmetry containing the contact axis [1–3]. Upon complete removal of the indenter, the radial and median cracks sometimes meet to form half-penny cracks (Fig. 1c). At high indentation loads, lateral cracks (Fig. 1d) may nucleate beneath the indenter and propagate sideways in a circular form, which may divert upwards towards the surface and cause chipping [1, 4–7]. In addition to the above commonly observed crack systems, other variant crack systems could also be produced by the Vickers indentation. They include secondary radial cracks (Fig. 1e) and shallow lateral cracks (Fig. 1f), which emanate from the edge of the indentation impression in some cases. The former usually occurs at small indentation loads in large-grained materials [5, 8] while the latter at high indentation loads [6, 7].

Finite Element (FE) analyses on indentation deformation and fracture have been performed by earlier researchers. Bhattacharya and Nix [9] studied the elasto-plastic micro-indentations on nickel, silicon and aluminium using axisymmetric elements. A similar analysis was performed by Laursen and Simo [10]. Both studies have showed that data such as the yielding zone and the contact area may be extracted more easily with the use of numerical simulations as compared to obtaining them from experiments. Other FE studies of elasto-plastic indentations using two-dimensional

---

*Author to whom all correspondence should be addressed.

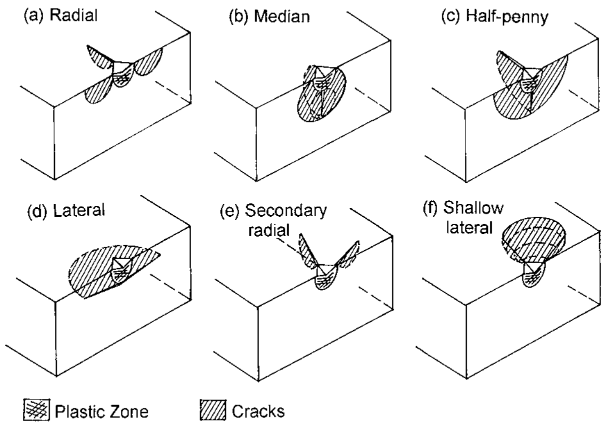

Figure 1 Primary (a, b, c and d) and secondary (e and f) crack systems produced by the Vickers indentation in brittle solids. (After Cook and Pharr [1]).

(2D) meshes include those of Olaf [11] and Cai [12, 13].

Three-dimensional (3D) FE simulations of the Vickers hardness test were made by Murakami and Matsuda [14], Giannakopoulos *et al.* [15, 16] and Zeng *et al.* [17–19]. These authors obtained the load-depth relations and extracted the mechanical properties of the test materials from the FE analyses, including hardness, yield stress, plastic zone size and strain hardening effects. The FE technique has also been applied to investigate indentation tests on thin films [20], coated systems [21, 22] and graded materials [23–25].

More recently, the FE technique has been extended to investigate the indentation fracture behaviour of solids. Using a combined variational and boundary integral method and by assuming that the crack takes the form of a surface semicircular crack in the median plane, Rabinvich and Sarin [26] investigated the development of stress-strain fields and plastic zone in both Vickers and Knoop indentations and deduced the crack length-indentation load relation for Knoop indentation of Si_3N_4. Assuming that the material was brittle elastic, the missing mesh technique was used by Niezgoda *et al.* [27] to follow the process of crushing fracture in stages; that is, the cracked elements were removed from the mesh and the model was re-meshed before subsequent analysis. The technique enabled a relatively coarse mesh to be used to yield reasonable stress distribution at full indentation load. However, no unloading results and associated cracking events were presented.

Larsson and Giannakopoulos [28] performed a detailed FE study, taking into account the strain hardening characteristics and pressure-sensitive inelastic properties of the material. Based on the development of the stress field in the material, they inferred the evolution of cracks during both loading and unloading of the indentation although the elements remained "uncracked" throughout the analysis.

Although brittle at room temperature, monolithic ceramics like alumina show evidence of the R-curve effect, i.e., a macroscopic increase in the fracture resistance as the crack grows [29–32]. Experimental studies further showed that for alumina, the source of this increased crack resistance is not located ahead of the crack tip but in the wake of the crack due to crack surface interactions [29–34]. In addition to the above, even though the cracked material is weak in tension when stressed across the crack surface, it could withstand compression and shear to certain extent. One way to model such post-failure behavior is to use the cohesive crack model proposed by Hillerborg *et al.* [35]. Lorca and Steinbrech [36] used such a model to simulate the the cracking behaviour of alumina ceramics in conventional fracture toughness tests. They reported that the model adequately describes the fracture processes of alumina in such tests. No post-failure behaviour has been considered in the FE works on indentation fracture thus far.

In this work, the cracking processes induced by micro- and macro-indentations of brittle solids are simulated by means of the FE analysis. Using alumina as the model material, suitable post-failure softening behaviours for cracked elements were incorporated in the model, including the ensuing anisotropic effect. The FE predictions are compared with experimental observations and other FEM results in the literature.

2. Methodology

Fig. 2 shows a schematic of the Vickers indentation. The Vickers indenter has an apex angle of 136° between opposite faces (Fig. 2b). Owing to the symmetrical nature of the Vickers indentation about the axes AA′, BB′, CC′ and DD′ (Fig. 2a), only one eighth of the indenter-material system was modelled.

The Vickers indentation process was modelled using the 3D mesh as shown in Fig. 3, which was generated using the software MSC/PATRAN [37]. The dimensions given indicate the size of the real specimen being modelled. The mesh comprises 9480 nodes and 8162 elements belonging to the first-order linear category. The

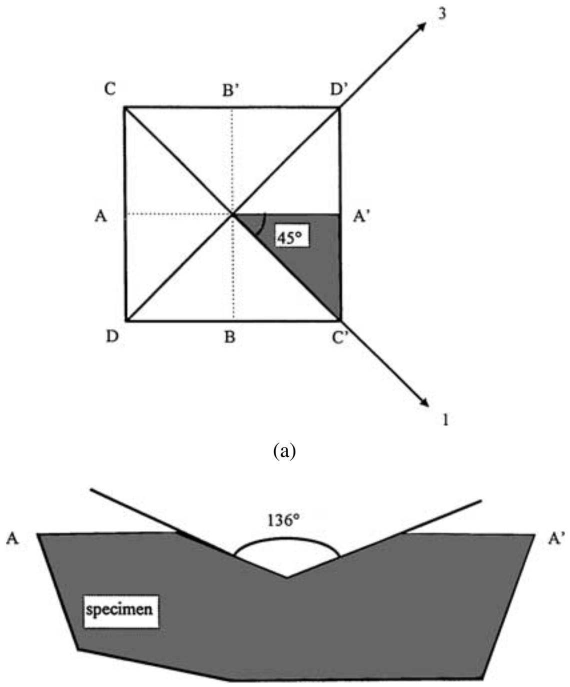

(a)

(b)

Figure 2 (a) Plain view and (b) side view of a Vickers indentation. Due to the eight-fold symmetry about the lines labelled in (a), only one eighth of the body need be modelled.

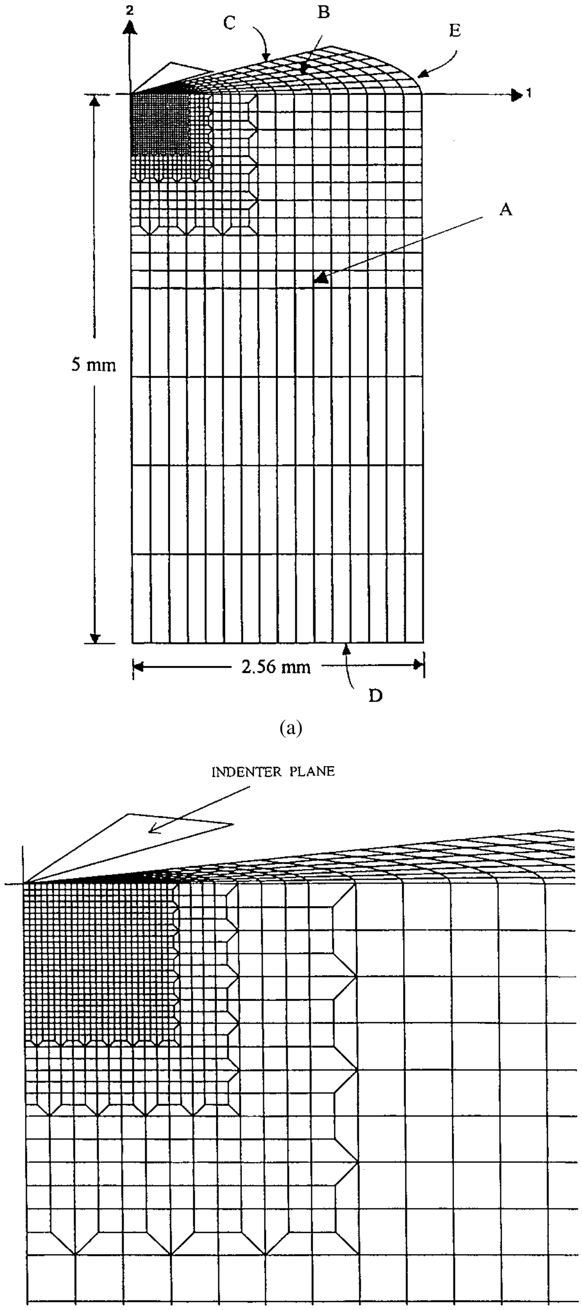

(a)

(b)

Figure 3 (a) The three dimensional mesh used for the finite element analysis of the indentation process. The external faces are labelled A, B, C, D and E. (b) shows a close-up view of the contact area between the indenter and the material being modelled.

mesh density is progressively higher in the region of interest that is close to the indentation impression. This is more clearly shown in Fig. 3b, which is a close-up of the region of interest, it being the indenter-material contact.

In Fig. 3a, the five free surfaces of the mesh are labelled A, B, C, D and E. The orientation of the indenter is such that the apex of the indentation impression lies on the edge between the top face (B) and the sectioned face of interest (A).

The boundary conditions applied on faces A, C and D are such that roller conditions apply, meaning that the displacements normal to the faces are zero and the tractions parallel to the faces are zero. As such, there is no vertical displacement on face D. Face E, which forms the curved surface surrounding the mesh of the indented material is traction-free. Face B is the indented surface and therefore, it contains the contact elements. The mesh and boundary conditions used closely resemble those used by Giannakopoulos *et al.* [15], who had performed extensive FE studies leading to the convincing reliability and trustworthiness of the mesh.

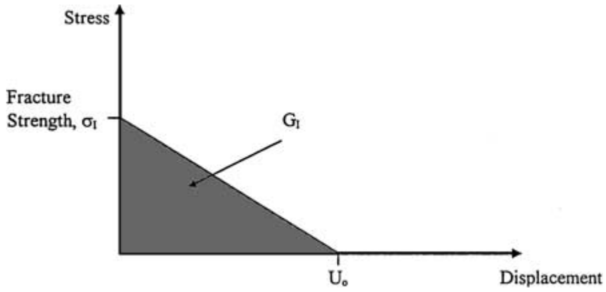

Figure 4 The mode I post-failure behaviour for the cracked elements strained across the crack used in the analysis. U_o is the crack normal displacement at which complete loss of strength takes place.

The Vickers indenter was assumed rigid in the analysis. The test specimen was modelled using the brittle cracking model available in ABAQUS/Explicit [38]. A simple Rankine criterion was used to detect crack initiation; that is, an element is deemed cracked when the maximum principal tensile stress exceeds the tensile strength σ_I of the brittle material being modelled, with the crack plane lying perpendicular to the direction of the maximum principal tensile stress.

Subsequent deformation behaviour of the cracked element is governed by the post-failure softening behaviour relating the transferred stress to the crack opening displacement U, which comprises both mode I and II. For Mode I post-failure softening behaviour, the cohesive crack model of Hillerborg *et al.* [35] was used, which satisfies the following conditions: the stress transferred through the crack equals σ_I when $U = 0$. The transferred stress drops to zero above a critical displacement U_o, i.e. $\sigma = 0$ when $U \geq U_o$. And, the area under the softening curve equals the fracture energy, G_I, i.e. the energy needed to create unit area of new crack surface. Fig. 4 illustrates the Mode I softening behaviour of a cracked element strained across the crack used in the present work. As for the shear (Mode II) softening, the default post-failure brittle shear behaviour was used; namely, the shear modulus of the cracked element was set to decrease linearly from the uncracked value at zero crack opening strain to 10^{-3} times of the uncracked value at a crack opening strain of 5×10^{-4}. Crack closing and reopening were allowed in the direction normal to the crack surface in the present work. It was assumed that the cracks close completely when the stress across them becomes compressive. The model also took into account the anisotropy effect created by cracking.

Although the aim of the present work is to investigate the cracking processes during the indentation of brittle solids, for purposes of comparison with experimental results on alumina, the material parameters used to define the model were kept as close as possible to the experimental values of high-purity alumina. The Young's modulus E was taken as 392 GPa and

Poisson's ratio as 0.27. The tensile strength of alumina was taken as 207 MPa [39]. The Mode I fracture energy G_I was estimated from the experimental indentation fracture toughness value of 3.9 MPa$\sqrt{}$m [40] from the following equation: $G_I = K_c^2(1-\nu^2)/E$, where E is the Young's modulus and ν the Poisson's ratio. This gives a value of 36 N/m for G_I for alumina. Knowing σ_I and G_I, the critical crack displacement U_o was obtained according to Fig. 4, giving a value of 0.34 μm. The ABAQUS/Explicit analysis required that the density value be given and this was specified as 3.99 g/cm^3, which is the theoretical density of alumina. Note that although alumina is brittle at room temperature, prior to cracking, it may deform plastically within a localised region underneath the indentation. This was ignored in the present work.

For the purpose of studying the effect of indentation load, two analyses were attempted, one representing the micro-indentation process and the other the macro-indentation process. The indentation process was simulated using ABAQUS/Explicit in two stages, namely, loading and unloading. In each stage, velocity boundary conditions were applied on the rigid indenter. As ABAQUS/Explicit treats problems dynamically, the analysis was performed in a quasi-static manner to ensure that inertia effects do not dominate and affect the solution. Loading was achieved by displacing the rigid indenter incrementally downwards to the maximum depth at full loading. To unload, the indenter was displaced upwards in incremental steps back to its original position. The maximum depths $h_{\max}$ for the micro- and macro-indentations were determined from indentation experiments on alumina using a load of 2 and 45 kgf, giving 6.3 and 28.6 μm, respectively.

The present analysis ignored the effect of friction on the indentation process. Cai [13] performed an FE analysis on the effect of friction in indentation hardness testing and found that frictional effects were negligible for Vickers indentations. Bower *et al.* [41], who worked on contact problems involving spherical indenters, also reached the same conclusion.

3. Results

3.1. Cracking processes in a micro-indentation test (low indentation loads)

Fig. 5 presents the results of the simulation for the micro-indentation of alumina with a load of 2 kgf

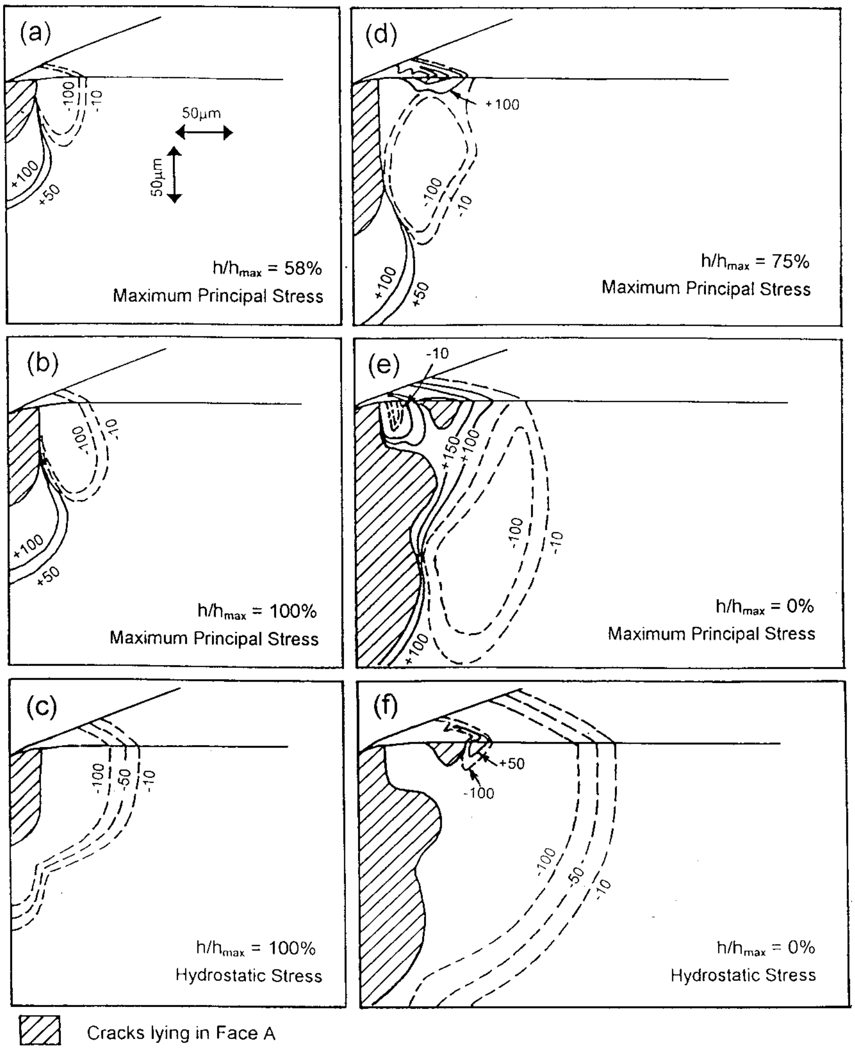

Figure 5 Iso-stress contour plots (in MPa) of the maximum principal stress on Face A at different stages of a micro-indentation process: (a) intermediate stage of loading ($h/h_{\max} = 58\%$); (b) full loading ($h/h_{\max} = 100\%$), (d) intermediate stage of unloading ($h/h_{\max} = 75\%$) and (e) full unloading $h/h_{\max} = 0\%$). (c) and (f) show the plots of hydrostatic stress (in MPa) at full loading and full unloading, respectively.

(corresponding $h_{\max} = 6.3$ μm), in the form of plots of maximum principal stress and hydrostatic stress as viewed on Face A, of which the top edge containing the apex of the indentation impression. The various stages of loading and unloading are characterised by the ratio of indentation depth h to the maximum depth $h_{\max}$ at full loading. Therefore, $h/h_{\max} = 100\%$ represents the stage at which the indenter has progressed to full loading while $h/h_{\max} = 0\%$ indicates that the indenter has reached full unloading.

Our simulation results show that upon loading, the material surrounding the indentation impression is placed in a state of hydrostatic compression while the material directly beneath the indenter is subjected to high tensile stresses acting across Face A, causing a median crack to form beneath the indenter (Fig. 5a). With increased indenter penetration, the hydrostatic compression region spreads outwards and the median crack extends deeper into the material. Fig. 5b and c show the plots of maximum principal stress and hydrostatic stress at full loading ($h/h_{\max} = 100\%$). There remains no sign of Palmqvist crack forming at the apex of the indentation impression at this stage. Therefore, in a micro-indentation, the median crack may form beneath the indenter. The crack, however, is unlikely to propagate to any significant extent as it is totally embedded in a zone of hydrostatic compression.

Upon unloading, the median crack continues to extend deeper into the material. At the same time, tensile stresses develop in the surface of the indentation impression as well as normal to Face A in the material beneath the apex of the indentation impression. The magnitude of the tensile stress, especially near the apex region, increases with further unloading. At about $h/h_{\max} = 75\%$, there is a good chance of a crack forming on Face A beneath the apex of the indentation impression, as the tensile stress (normal to Face A) there exceeds the fracture strength of the material (Fig. 5d). The crack would produce a radial trace on the top surface of the material, forming a Palmqvist crack.

The next few stages of unloading show the continued but gradual spread of the median and Palmqvist cracks as the elements adjacent to them were stressed to fracture progressively. Fig. 5e and f show the plots of maximum principal stress and hydrostatic stress on Face A at full unloading ($h/h_{\max} = 0\%$). The tensile stress fields emulated from the surface region near the apex of the indentation and that from deep down in the material beneath the indentation impression have extended considerably and actually overlapped, providing the driving force for the median and Palmqvist cracks to grow and link up. However, since the magnitude of tensile stresses in the interconnecting region remains lower than the fracture strength of the material and since this region is contained in the bigger cage of hydrostatic compression produced by the indentation (Fig. 5f), it is possible that both the median and Palmqvist cracks may not link up eventually. Judging from the affected elements in Fig. 5e, the size of the Palmqvist crack is estimated at about 50 to 80 μm for pure alumina, which agrees reasonably with our experimental observation.

3.2. Cracking processes in a macro-indentation test (high indentation loads)

The results of simulation of the macro-indentation of alumina with a load of 45 kgf (corresponding $h_{\max} = 28.6$ μm) are shown in Fig. 6. Shortly after loading, the tensile stress (normal to Face A) in the material beneath the indenter exceeds the fracture strength of the material, causing the median crack to form on Face A. At intermediate stages of loading (e.g., $h/h_{\max} = 57\%$), the material beneath the apex of the indentation also experiences sufficiently high tensile stress to enable a Palmqvist crack to nucleate there (Fig. 6a). At full indentation loading ($h/h_{\max} = 100\%$), the region of high tensile stresses (i.e. >207 MPa; normal to Face A) on Face A has spread considerably (Fig. 6b), enabling the Palmqvist and median cracks formed earlier to join up to form a half-penny crack. However, the half-penny crack so formed is stable as it is embedded in a cage of high hydrostatic compression generated by the indentation (Fig. 6c).

Similar to the micro-indentation, large tensile stresses develop in the surface of the indentation impression during initial stages of unloading. An interesting phenomenon occurs on further unloading; that is, a sectorial annulus of tensile stressed material evolves, separating the cracked material beneath the indenter from the uncracked material farther away (Fig. 6d). (The shape of the annulus was confirmed by examining its cross section on Face B.) The annulus starts from the surface region along the periphery of the indentation impression, which penetrates further into the material on continued unloading. A check was made as regard the direction of maximum tensile stress in the annulus in this figure. It was found that it is predominantly circumferential on Face A, i.e. normal to Face A, with the radial component increasing as one moves away from Face A along the perimeter of the annulus.

Fig. 6e and f show, respectively, the plots of maximum principal stress and hydrostatic stress at full unloading. Note the high tensile stress in the surface region along the outer periphery of the tensile annulus (Fig. 6e) and the vivid but smaller annulus of hydrostatic tension adjacent to the half-penny crack, i.e. along the inner periphery of the above-described tensile annulus (Fig. 6f). The high tensile stresses generated by the unloading thus provide the driving force for further propagation of the half-penny crack as well as the formation of new crack systems, such as deep and shallow lateral cracks. Judging from the lateral reach of the larger tensile annulus, the length of radial crack as observed from the specimen surface is estimated at about 200–300 μm at full unloading of a typical macro-indentation test. This is consistent with our experimental observation.

4. Discussion

The present work shows that during the indentation test of brittle solids at low loads, median and Palmqvist cracks nucleate separately; that is, median cracks nucleate at later stages of loading while Palmqvist cracks form only during the unloading stage of the

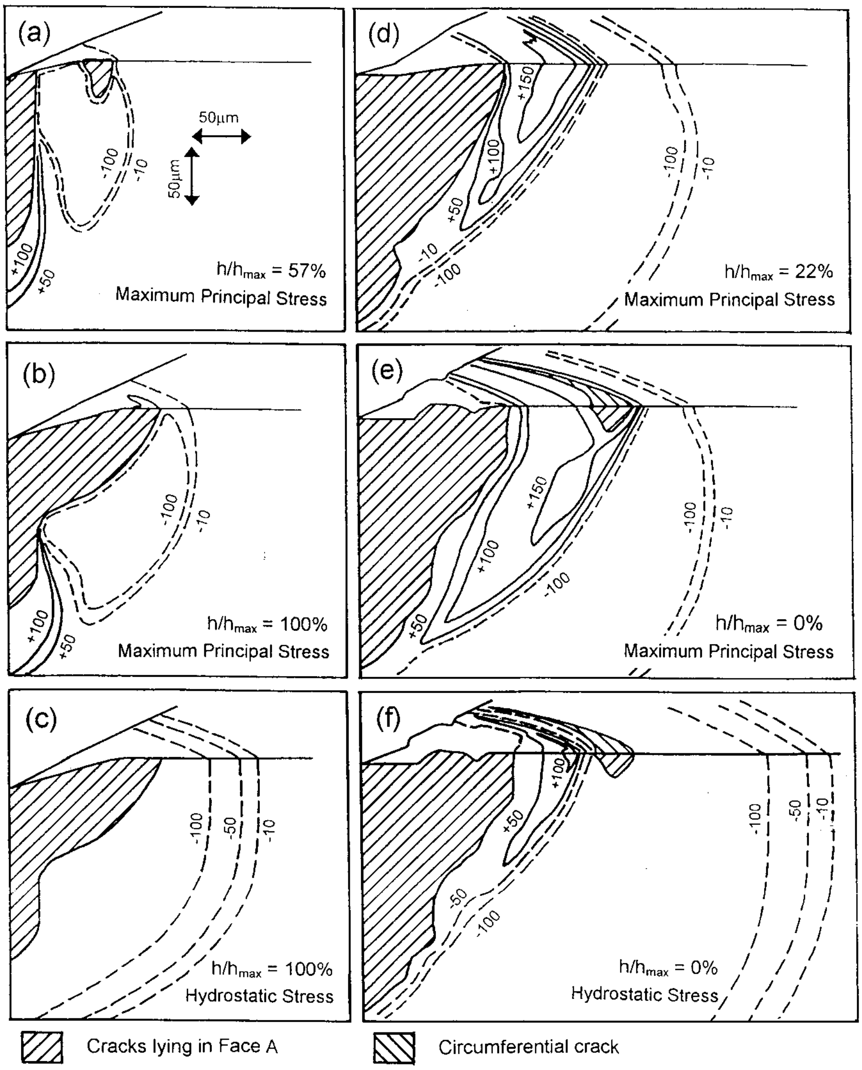

Figure 6 Iso-stress contour plots (in MPa) of the maximum principal stress on Face A at different stages of a macro-indentation process: (a) intermediate stage of loading ($h/h_{\max} = 57\%$), (b) full loading ($h/h_{\max} = 100\%$), (d) intermediate-to-later stage of unloading ($h/h_{\max} = 22\%$) and (e) full unloading ($h/h_{\max} = 0\%$). (c) and (f) show the plots of hydrostatic stress (in MPa) at full loading and full unloading, respectively.

micro-indentation. However, they are unlikely to grow to any appreciable extent and hence may not link up to form half-penny cracks during the micro-indentation at low indentation loads. In contrast, at high indentation loads (i.e. in a macro-indentation), the median and Palmqvist cracks nucleate separately and eventually join up to form a half-penny crack during the loading stage. This prediction is consistent with experimental results reported by earlier researchers [1, 42–44], who showed that both median and Palmqvist cracks nucleated separately though their propagation was rather stunted during loading in the micro-indentation test and that there is a gradual change from Palmqvist cracks to half-penny median cracks as the indentation load is increased [1, 42].

The present work also shows that large tensile stresses develop in the surface of the indentation impression during the unloading of both the micro- and macro-indentations (Figs 5 and 6). These tensile stresses are likely sources for microfracture or spallation of grains from the surface of indentation impression during the unloading.

More interestingly, the present work shows that a sectorial annulus of tensile stressed material develops during unloading in the macro-indentation, separating the cracked material beneath the indentation impression and the surrounding uncracked material. The annulus starts from the surface region along the periphery of the indentation impression, penetrating downwards into the material on continued unloading. Although a tensile region in between the elasto-plastic boundary has been predicted during unloading of elasto-plastic indentations [15–19, 24, 25], a fully developed annular tensile region has never been reported thus far. Another major difference between the present result and those based on elasto-plastic indentations is that in the brittle crack model, the tensile stresses and hence the ensuing median cracks are found to spread deeper into the material, especially along the central column of material beneath the indentation impression.

Since the material is assumed to behave in a completely elastic and isotropic manner prior to fracture under the indentation, the post-failure softening behaviour of the cracked body beneath the indenter and the ensuing anisotropic elastic recovery during unloading are expected to dominate the inelastic behaviour of the material being modelled.

The present result can be visualised by treating the unloading event as superimposing the corresponding tension to the affected material. Two phenomena dominate adjacent to the cracked elements; namely, not only are the crack surfaces unable to take tensile loads as one unloads but also, due to the effect of Poisson's ratio, the superimposed tensile stress parallel to the crack surface will cause the material adjacent to the crack surface to contract inwards. As the latter effect is restricted by the uncracked elements above and below the crack, this would cause tensile stresses normal to the plane of the crack to be set up in the uncracked elements immediately above and below the crack, resulting in the preferential spreading of the crack. This explains the preferential penetration of the median crack deeper into the material during unloading in both the micro- and macro-indentations observed in the present work. The evolution of the larger annulus of predominantly circumferential tensile stressed material during unloading of the macro-indentation, separating the cracked material beneath the indentation impression and the surrounding uncracked material, can also be explained likewise.

The formation of the smaller annulus of hydrostatic tension adjacent to the central cracked body can be understood from the different elastic unloading behaviours between the cracked material beneath the indenter and the surrounding uncracked material. For the cracked material, the elastic unloading is affected by the presence of the half-penny cracks, which occur in the median plane of the indentation. That is, any large superimposed tension arising from unloading is only possible in the plane of the crack surface but not perpendicular to it. In other words, for unloading a given amount of hydrostatic compression in the cracked material, a larger superimposed tension, hence the resultant spring back, is expected in both the radial and axial directions than in the circumferential direction. This is not so for the uncracked body farther away, where a more uniform state of elastic spring back occurs. This difference in the elastic unloading behaviour is accentuated in two locations. The first is the boundary region between the cracked and uncracked bodies, where the large superimposed tensions in both the radial and axial directions are expected to spill over to the adjacent material which, when superimposed onto the large crack-opening (i.e. circumferential) mode stress there, produces the annulus of hydrostatic tension seen in Fig. 6f. The second location is the surface region of the annulus where any superimposed tension can only be applied along the radial direction but not the axial direction due to the free surface effect. This explains the start of the tensile annulus at the surface region and its subsequent spreading downwards into the material on continued unloading (Fig. 6d and e).

It is evident from the present work that the tensile stresses arising from the unloading in the macro-indentation would provide the driving force for the propagation of existing cracks and the formation of new crack systems. For instance, the high tensile stresses spreading over the surface region of the indentation

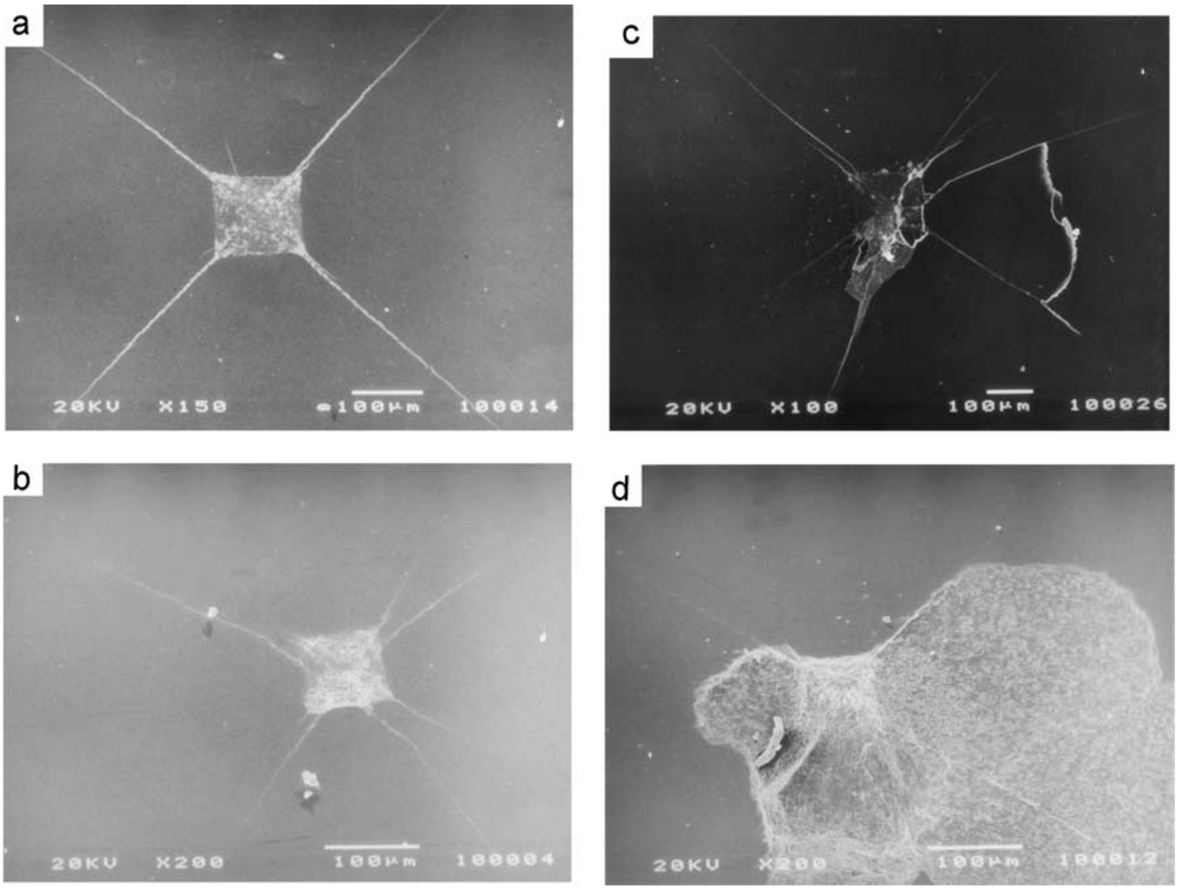

Figure 7 Examples of cracks in alumina produced by macro-indentations: (a) well-defined radial cracks (indentation load = 30 kgf; grain size = 1.9 μm); (b) secondary radial cracks (15 kgf; 1.9 μm), (c) shallow lateral cracks (45 kgf; 0.9 μm) and (d) deep lateral cracks and chipping (45 kgf; 1.9 μm).

impression (Fig. 6e and f) may lead to micro-fracture via grain spallation. The high tensile stress in the surface region along the outer periphery of the larger annulus would also cause shallow lateral cracks or secondary radial cracks to form at the periphery of the indentation impression. Similarly, the annular tensile region deep in the material beneath the indentation impression would cause additional cracks to nucleate deep within the material and existing cracks to propagate and link up, leading to lateral cracking from within the material.

Examples for the above are provided in Fig. 7, which were obtained by the present authors during macro-indentation tests of pure alumina. Fig. 7a shows well-behaved radial cracks at apexes of the indentation impression, while Fig. 7b to d show secondary radial cracks, shallow and deep lateral cracks and chipping produced by the macro-indentation process. Note also the evident of grain spallation at the surface and along the periphery of the indentation impressions in these figures. The formation of both shallow and deep lateral cracks and associated chipping around the indentation impressions at high indentations loads were also documented by Cook *et al.* [1, 6, 7], Lawn *et al.* [4] and Anstis *et al.* [5], while grain spallation on surfaces of indentation impression during unloading was reported by Anstis *et al.* [5] and Muchtar and Lim [40].

In the micro-indentation, indications of the initial development of the annular tensile region near the surface region can also be detected upon full unloading (Fig. 5e). However, at sufficiently low loads, the annular tensile region could not develop substantially. This explains the absence of deep lateral cracks and other secondary cracks in the micro-indentation.

5. Concluding remarks

The evolution of the maximum principal stress and hydrostatic stress and the potential crack nucleation and propagation events during indentation of brittle solids have been investigated by means of the FEM, using elements exhibiting cohesive post-failure behaviour and alumina as the model material. The results show that at low indentation loads, median cracks nucleate at full loading while Palmqvist cracks nucleate only during the unloading stage and that they may or may not join up to form a half-penny crack depending on the indentation load. In contrast, at high indentation loads, both median and Palmqvist cracks nucleate separately and join up to form a half-penny crack during the loading stage. The result further shows that an annular tensile region develops during intermediate to later stages of unloading of the macro-indentation, promoting additional crack systems to form in the indentation test. Although similar tensile stress patterns are produced in the surface region adjacent to the indentation impression, such an annulus of tensile stress and hydrostatic tension does not develop substantially in the micro-indentation, which explains the absence of lateral cracking in the micro-indentation.

Since no plasticity is assumed in the present work and since most of the cracking events occur during the unloading stage of the indentation, the present results suggest that the stresses produced by the mismatch in elastic recovery between the cracked and uncracked bodies during the unloading stage are the main driving force for the fracture events in the indentation of brittle solids. This is especially so at high indentation loads, where an annulus of tensile stressed material evolves from the surface region along the periphery of the indentation impression, which penetrates deeper into the material on continued unloading. This provides a favourable condition for existing cracks to grow and link up and the formation of other crack systems, such as swallow lateral cracks, deep lateral cracks, and secondary radial cracks, etc. The predicted cracking behaviours of brittle solids under indentation loading agree fairly well with experimental results reported in the literature and obtained by the present authors.

References

1. R. F. COOK and G. M. PHARR, *J. Amer. Ceram. Soc.* **73** (1990) 787.
2. B. R. LAWN and E. R. FULLER, *J. Mat. Sci.* **10** (1975) 2016.
3. B. R. LAWN, A. G. EVANS and D. B. MARSHALL, *J. Amer. Ceram. Soc.* **63** (1980) 574.
4. B. R. LAWN, M. V. SWAIN and K. PHILLIPS, *J. Mater. Sci.* **10** (1975) 1236.
5. G. R. ANSTIS, P. CHANTIKUL, B. R. LAWN and D. B. MARSHALL, *J. Amer. Ceram. Soc.* **64** (1981) 533.
6. R. F. COOK, E. G. LINIGER, M. R. PASCUCCI, *J. Hard Mater.* **5** (1990) 191.
7. R. F. COOK, M. R. PASCUCCI and W. H. RHODES, *J. Amer. Ceram. Soc.* **73** (1990) 1873.
8. R. F. COOK, B. R. LAWN and C. J. FAIRBANKS, *J. Amer. Ceram. Soc.* **68** (1985) 604.
9. A. K. BHATTACHARYA and W. D. NIX, *Int. J. Solids Structures* **24** (1988) 881.
10. T. A. LAURSEN and J. C. SIMO, *J. Mater. Res.* **7** (1992) 618.
11. J. M. OLAF, in Proceedings of the 1st International Conference on Contact Mechanics, Southampton, 1993, p. 69.
12. X. J. CAI, *Mater. Sci. Lett.* **11** (1992) 1527.
13. *Idem., ibid.* **12** (1993) 301.
14. Y. MURAKAMI and K. MATSUDA, *Transactions of the ASME* **61** (1994) 822.
15. A. E. GIANNAKOPOULOS, P.-L. LARSSON and R. VESTERGAARD, *Int. J. Solids Structures* **31** (1994) 2679.
16. A. E. GIANNAKOPOULOS and P.-L. LARSSON, *Mechanics of Materials* **25** (1997) 1.
17. K. ZENG, A. E. GIANNAKOPOULOS and D. J. ROWCLIFFE, *Acta Metall. Mater.* **43** (1995) 1935.
18. *Idem., ibid.* **43** (1995) 1945.
19. K. ZENG, E. SODERLUND, A. E. GIANNAKOPOULOS and D. J. ROWCLIFEE, *Acta Mater.* **44** (1996) 1127.
20. L. GAN, B. BEN-NISSAN and A. BEN-DAVID, *Thin Solid Films* **290/291** (1996) 362.
21. H. F. WANG, X. YANG, H. BANGERT, P. TORZICKY and L. WEN, *ibid.* **214** (1992) 68.
22. H. F. WANG and H. BANGERT, *Mater. Sci. Eng.* **A163** (1993) 43.
23. S. SURESH, A. E. GIANNAKOPOULOS and J. ALCALA, *Acta. Mater.* **45** (1997) 1307.
24. A. E. GIANNAKOPOULOS and S. SURESH, *Int. J. Solid Structures* **34** (1997) 2393.
25. *Idem., ibid.* **34** (1997) 2357.
26. V. L. RABINOVICH and V. K. SARIN, *Mater. Sci. Eng.* **A206** (1996) 208.
27. T. NIEZGODA, J. MALACHOWSKI and M. BONIECKI, *Ceramics International* **24** (1998) 359.
28. P.-L. LARSSON and A. E. GIANNAKOPOULOS, *Mater. Sci. Eng.* **A254** (1998) 268.
29. R. KNEHANS and R. W. STEINBRECH, *J. Master. Sci. Lett.* **1** (1982) 327.
30. R. W. STEINBRECH, R. KNEHANS and W. SCHAARWACHTER, *J. Mater. Sci.* **18** (1983) 265.
31. M. V. SWAIN, *J. Mater. Sci. Lett.* **5** (1986) 1313.
32. P. L. SWANSON, C. J. FAIRBANKS, B. R. LAWN,

Y. W. MAI and B. J. HOCKEY, *J. Amer. Ceram. Soc.* **70** (1987) 279.

33. A. REICHL and R. W. STEINBRECH, *ibid.* **71** (1988) C-299.
34. E. INGHELS, A. H. HEUER and R. W. STEINBRECH, *ibid.* **73** (1990) 2023.
35. A. HILLERBORG, M. MODEER and P. E. PETERSON, *Cement Concrete Res.* **6** (1976) 773.
36. J. LORCA and R. W. STEINBRECH, *J. Mater. Sci.* **26** (1991) 6383.
37. MSC/PATRAN User's Manual, Version 5.0. (The MacNeal-Schwendler Corporation, Colorado Boulevard, Los Angeles, USA, 1996).
38. ABAQUS/Explicit User's Manual, Version 5.7. Hibbitt, (Karlsson and Sorenson, Inc., Pawtucket, Rhode Island, USA, 1997).
39. ASM Guide to Engineering Materials, Vol. 1, 1986, p. 64.
40. A. MUCHTAR and L. C. LIM, *Acta Mater.* **45** (1998) 1683.
41. A. F. BOWER, N. A. FLECK, A. NEEDLEMAN and N. OGBONNA, *Proc. R. Soc. Lond.* **A441** (1993) 997.
42. K. M. LIANG, G. ORANGE and G. FANTOZZI, *J. Mater. Sci.* **25** (1990) 207.
43. D. K. SHETTY, I. G. WRIGHT, P. N. MINCER and A. H. CLAUER, *ibid.* **20** (1985) 1873.
44. P. OSTOJIC and R. McPHERSON, *Int. J. Fracture* **33** (1987) 297.

Received 1 February
and accepted 24 September 2002